PNAS RESEARCH ARTICLE | BIOPHYSICS AND COMPUTATIONAL BIOLOGY OPEN ACCESS

Volumetric imaging of the 3D orientation of cellular structures with a polarized fluorescence light-sheet microscope

Talon Chandler[a,b,1,2], Min Guo[c,d,1,2], Yijun Su[d,e,f], Jiji Chen[e], Yicong Wu[d], Junyu Liu[c], Atharva Agashe[g], Robert S. Fischer[h], Shalin B. Mehta[a,b,i], Abhishek Kumar[i], Tobias I. Baskin[j,k], Valentin Jaumouillé[l], Huafeng Liu[c], Vinay Swaminathan[m,n], Amrinder S. Nain[g], Rudolf Oldenbourg[i], Patrick J. La Riviere[b,k], and Hari Shroff[d,e,f,k]

Affiliations are included on p. 11.

Edited by Sophie Brasselet, Institut Fresnel Marseille, Marseille, France; received April 2, 2024; accepted January 6, 2025, by Editorial Board Member Hui Cao

Polarized fluorescence microscopy is a valuable tool for measuring molecular orientations in biological samples, but techniques for recovering three-dimensional orientations and positions of fluorescent ensembles are limited. We report a polarized dual-view light-sheet system for determining the diffraction-limited three-dimensional distribution of the orientations and positions of ensembles of fluorescent dipoles that label biological structures. We share a set of visualization, histogram, and profiling tools for interpreting these positions and orientations. We model the distributions based on the polarization-dependent efficiency of excitation and detection of emitted fluorescence, using coarse-grained representations we call orientation distribution functions (ODFs). We apply ODFs to create physics-informed models of image formation with spatio-angular point-spread and transfer functions. We use theory and experiment to conclude that light-sheet tilting is a necessary part of our design for recovering all three-dimensional orientations. We use our system to extend known two-dimensional results to three dimensions in FM1-43-labeled giant unilamellar vesicles, fast-scarlet-labeled cellulose in xylem cells, and phalloidin-labeled actin in U2OS cells. Additionally, we observe phalloidin-labeled actin in mouse fibroblasts grown on grids of labeled nanowires and identify correlations between local actin alignment and global cell-scale orientation, indicating cellular coordination across length scales.

polarized fluorescence microscopy | biophysical | imaging | inverse problem

Significance

Cells rearrange their constituent molecules to create dynamic, three-dimensional structures critical to their function. Muscle and brain tissue, for example, rely on anisotropic chemical, mechanical, and electrical properties that often coincide with optical anisotropies revealed by polarization-based microscopy, including polarized fluorescence. While most such microscopes are limited to measuring a subset of orientation parameters, we built a microscope that can assess the complete 3D orientation and position distribution of ensembles of fluorescent molecules. We demonstrate and validate the technique by imaging labeled membrane, cellulose, and actin, proceeding to study cell growth on nanowire grids. We find that actin orientations at the smallest measurable scale are correlated with the large-scale orientation of the entire cell, revealing unexpected coordination across scales.

Measuring the orientation of fluorescent molecules can provide valuable insights into architecture, order, and dynamics in biology and material science (1). By tagging a biological structure with a fluorescent reporter that rotates along with the structure of interest, biologists can deduce biophysical dynamics by measuring the orientation of the fluorescent molecule. A large fraction of fluorescent reporters absorb and emit light via an electronic dipole moment, i.e. in a polarized anisotropic pattern, so biologists can use optical microscopy to examine a fluorophore's excitation and emission patterns to draw conclusions about the fluorescent reporter's orientation.

Many techniques make ensemble measurements of diffraction-limited regions. By making multiple measurements of the same region under variably polarized illumination and/or detection, then calculating each region's fluorescence anisotropy (2, 3), researchers can draw conclusions about membrane labeling (4, 5), septin dynamics (6–8), nuclear pore proteins (9), force orientations (10, 11), and liquid crystals (12, 13). Recent engineering efforts have improved the spatial resolution (14), signal-to-noise ratio (SNR) (15), and out-of-plane resolution (16) of these ensemble measurements. While some of these studies make assumptions about their samples to estimate three-dimensional orientations, to our knowledge none simultaneously measure orientation and position in three dimensions.

More recently, a collection of single-molecule measurement techniques has enabled researchers to measure more parameters, including three-dimensional position, orientation, and rotational dynamics, from a sparse set of emitters. These techniques have been used to distinguish ordered and unordered biomolecular condensates (17), follow DNA conformation changes under tension (18), and capture dynamics of amyloid fibrils (19), myosin (20), membrane (21), and actin (22, 23). Despite considerable success, these single-molecule efforts face challenges beyond those faced by all fluorescence polarization techniques, with tighter constraints on throughput, SNR, and choice of emitters, constraining their wider adoption.

This article is a PNAS Direct Submission. S.B. is a guest editor invited by the Editorial Board.

[1]T.C. and M.G. contributed equally to this work.

[2]To whom correspondence may be addressed. Email: talon.chandler@czbiohub.org or guom@zju.edu.cn.

This article contains supporting information online at https://www.pnas.org/lookup/suppl/doi:10.1073/pnas.2406679122/-/DCSupplemental.

Published February 21, 2025.

After surveying the field, we identified an unmet need for measurements that can be used to recover the three-dimensional orientation and position of fluorescent ensembles. We reasoned that a dual-view light-sheet system (24) should provide an excellent platform for measuring the orientation of fluorescent ensembles because of its two excitation and detection arms, enabling diverse illumination and detection polarizations alongside improved axial spatial resolution.

In our initial iteration, we added liquid crystal polarizers to both excitation arms of an existing dual-view light sheet system and attempted to recover the predominant orientation of fluorophores from within each diffraction-limited volume (25). We found it challenging to merge a single-molecule description of the image formation process with the pixel-wise fluorescence anisotropy methods that are common in ensemble measurements, and we were unable to resolve orientational ambiguities. Inspired by the success of diffusion-tensor MRI (dMRI) (26) and its high-angular resolution extensions (27), we developed a coarse-grained formalism for spatio-angular fluorescence microscopy (28–30) that we applied to our instrument. The formalism led us to a set of critical engineering insights:

- unlike dMRI, fluorescence microscopes are spatio-angularly coupled, i.e. the orientation of molecules affects the spatial point-response function,
- in addition to the widely known spatial diffraction limit, fluorescence microscopes face angular diffraction limits set by the physics of dipolar excitation, dipolar emission, and the microscope's geometry, and
- our initial design had a hole in its spatio-angular transfer function, a null function, which caused the observed orientational ambiguities.

In this article, we describe the key element of our formalism, the orientation distribution function (ODF), and how we have used it to model our three-dimensional spatio-angular fluorescence microscope. We use ODFs to formulate a forward model that lets us identify spatio-angular holes in our designs. We introduce a solution, light-sheet tilting, and we demonstrate that it resolves the ambiguity with the same number of measurements. Subsequently, we describe our observations of membranes, cell walls, and actin in cells grown on a coverslip and on grids of nanowires. We close by inspecting spatio-angular correlations across length scales, and we discuss future directions for this field.

1. Results

1.1. ODFs Are Coarse-Grained Models of Fluorescent Dipoles That Label Biological Structures. Fig. 1*A* depicts the class of fluorescent objects that we are trying to recover—extended objects containing ensembles of molecules that move and rotate in three dimensions and whose spatial and orientational properties we wish to characterize within diffraction-limited regions. Assuming that each molecule's excitation and emission dipole moments are aligned—a reasonable approximation for many fluorophores (31)—we can summarize each fluorophore with a single axis. We can further summarize all of the molecules within a diffraction-limited region with an object ODF, a spherical function that we depict as a surface with a radius proportional to the number of dipoles oriented along each direction. Fluorescent dipoles that label structures are caught in angular potentials where they rotate during a measurement, contributing to the width and angular-diffusive smoothness of the corresponding ODF. Note that fluorescent dipoles are excited and emit symmetrically about their dipole axes which means that 1) we can depict their dipole moments as axes instead of vectors, and 2) their corresponding ODFs are always antipodally symmetric (*SI Appendix*, section 8.5).

Object ODFs can describe a wide range of realistic 3D dipole distributions (Fig. 1*B*). For example, dipoles that rotate freely in solution have an isotropic (spherical) ODF, dipoles that lie flat in the plane of a membrane have a pancake-shaped ODF with more tightly constrained dipoles having correspondingly flatter ODFs, dipoles that are oriented normal to a membrane have a dumbbell-shaped ODF with more tightly constrained dipoles having correspondingly sharper ODFs, and dipoles that lie parallel to multiple axes within a diffraction-limited region have a multilobed ODF.

We have developed a quasi-static model of fluorescent ensembles, where angular diffusion during a measurement is included within each object ODF, and object ODFs do not change during a measurement. While this model is reasonably accurate for many polarized fluorescence experiments, it ignores effects from fluorescence lifetime, saturation, and spatial diffusion among others. For a complete account of the assumptions leading to our quasi-static model of fluorescent ensembles, we direct readers to *SI Appendix*, section 6 and (30). Additionally, we assume that all excited molecules emit equally brightly.

Our primary strategy for generating contrast between different object ODFs is orientation-selective excitation (Fig. 1*C*). Orientation-selective excitation uses polarized light to excite a subset of an object ODF's molecules, creating a distribution of excited molecules that we call an excited ODF. Linearly polarized illumination excites an ensemble of dipole absorbers with an efficiency that is proportional to $\cos^2\theta$, where θ is the angle between the illumination polarization axis and the excitation dipole moment of individual fluorophores in the distribution. Hence, the excited ODF is the product of the object ODF and the excitation's $\cos^2\theta$ efficiency. When more molecules are excited, more fluorescence can be emitted and collected, so the largest signals will come from object ODFs that are parallel to the illumination polarization. Light is polarized perpendicular to its direction of propagation, so we preferentially excite emitters whose dipole moments are perpendicular to the optical axis of the excitation objective.

Once we have an excited ODF, we can use orientation-selective detection to generate more contrast (Fig. 1*D*). Ensembles of excited fluorophores emit polarized anisotropic patterns that report their underlying excited ODF. Many instruments use polarization filters/splitters to probe these polarization patterns, but here we rely only on the intensity anisotropy of the emission pattern—a $\sin^2\phi$ intensity distribution where ϕ is the angle between the emission dipole moment and the emission direction. By detecting light with an objective that does not collect light from the entire half space (numerical aperture < index of refraction), we preferentially detect emitters whose dipole moments are perpendicular to the optical axis of the detection objective. Therefore, we will measure the largest signals from excited ODFs that lie entirely in the plane perpendicular to the detection objective's optical axis.

We generate additional contrast by measuring, modeling, and inverting orientation-dependent point spread functions (Fig. 1*E*). A dipole's polarized emissions interfere to create point spread functions that encode information about the dipole's orientation. For example, an axial dipole generates a donut-shaped irradiance pattern spread over a larger area on the detector

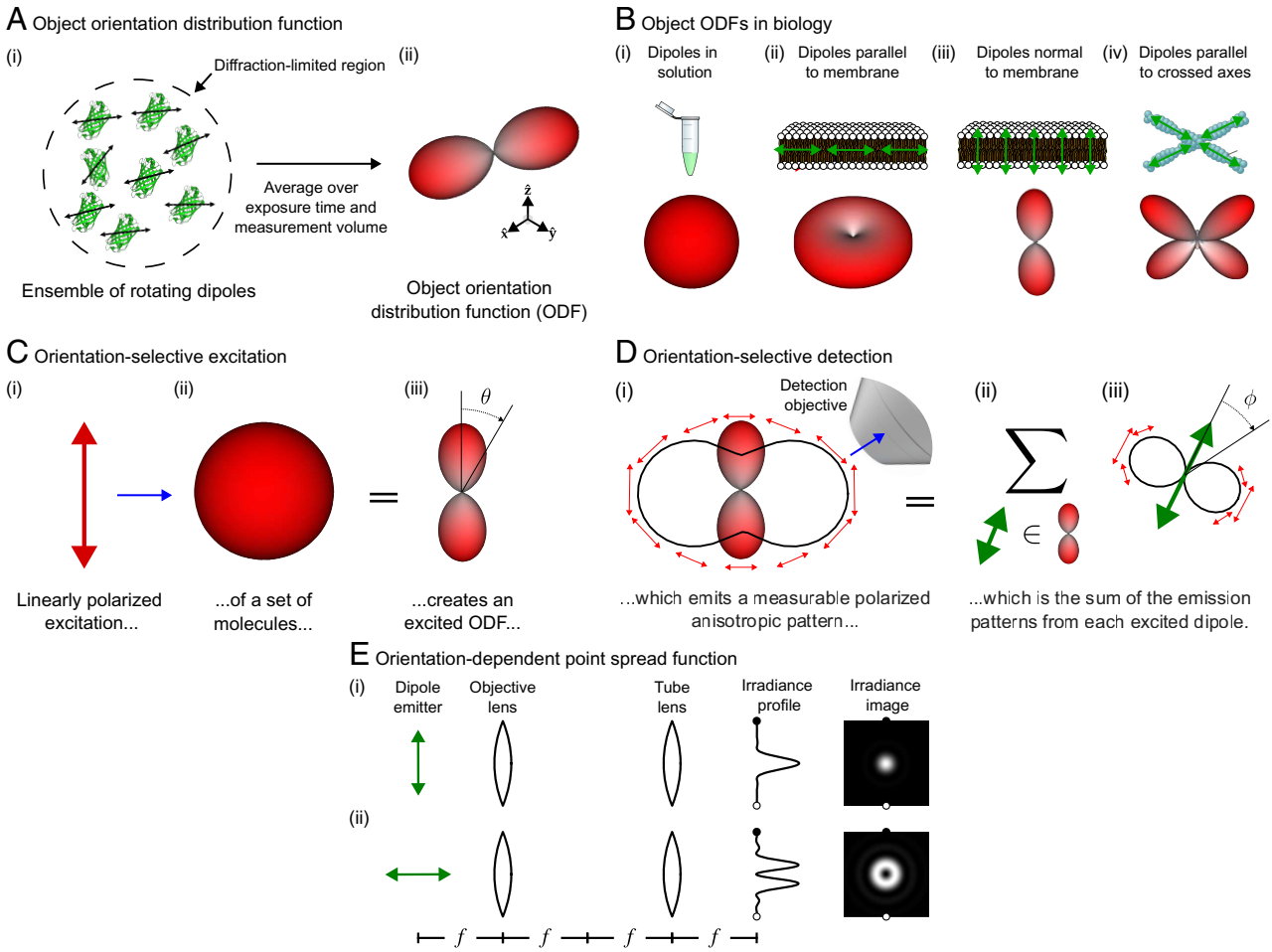

Fig. 1. Orientation distribution functions (ODFs) can model ensembles of oriented fluorophores that label biological structures, their excitation, and their detection. (*A*) (*i*) Fluorescent samples consist of molecules that move and rotate in three dimensions (e.g. green fluorescent protein molecules pictured), and many of the most common fluorescent molecules' excitation and emission behavior can be described by a single 3D dipole axis (double-sided black arrows overlaid on each molecule). Our instrument excites and measures emissions from diffraction-limited regions that contain many fluorescent molecules (dashed circle), so (*ii*) we simplify our model of individual emitters to a coarse-grained model called an object ODF. An ODF is a spherical function that we depict as a surface with a radius proportional to the number of dipoles in the measurement volume that are oriented along each direction. (*B*) Dipole distributions (*Top* row) can be modeled by object ODFs (*Bottom* row). (*i*) Fluorescent dipoles in solution typically rotate rapidly during the measurement time of fluorescent microscopes, so the corresponding ODFs are isotropic, depicted as a surface with constant radius. (*ii–iv*) When fluorescent dipoles (green double-sided arrows) are spatially and rotationally constrained, their corresponding object ODFs report the orientation of labeled biomolecules. (*C*) We can probe an object ODF by exciting a subset of molecules with polarized light. For example, when (*i*) linearly polarized light (red arrow) illuminates (blue arrow) an (*ii*) isotropic object ODF, (*iii*) the resulting subset of excited molecules, which we call an excited ODF, will have a $\cos^2\theta$ dependence where θ is the angle between the incident polarization and the excitation dipole moment of the individual fluorophores in the distribution. Selectively exciting molecules creates contrast between different object ODFs. (*D*) We can create more contrast by selectively detecting an excited ODF's emissions. (*i*) An excited ODF (red glyph) emits a polarized emission pattern (red arrows, perpendicular to the emission direction) that is anisotropic (solid black line, radius is proportional to the emitted power along each direction) which encodes information about the excited ODF. Selectively detecting emissions with an objective (blue arrow) creates contrast between excited ODFs. (*ii*) The emission pattern in (*i*) is the sum (Σ) of the emissions from each dipole (green double-sided arrow) in ($\in$) the excited ODF. (*iii*) Similar to (*i*), each dipole emits a polarized emission pattern that is anisotropic, with each dipole emitting in a $\sin^2\phi$ intensity pattern where ϕ is the angle between the emission dipole moment and the emission direction. (*E*) Each dipole emitter (green arrow) creates a measurable orientation-dependent point spread function. For example, in a 4*f* imaging system, where *f* indicates a focal length, (*i*) a transverse dipole emitter creates a pattern similar to the familiar Airy disc, while (*ii*) an axial dipole emitter creates a donut-shaped point spread function (shown here with normalized maximum irradiance). Black and white dots indicate the same points in the profile and image views.

than a transverse dipole. These effects lead to coupling between the angular distribution of dipoles and the spatial point spread function of the imaging path. We model these effects using a spatio-angular point spread function.

A single ODF can be modeled mathematically as a function on a sphere, where the value of the function along a specific direction corresponds to the number of dipoles along that direction. This means that we can write arbitrary ODFs as $f(\hat{\mathbf{s}}_o)$, where $\hat{\mathbf{s}}_o$ is a coordinate on a two-dimensional sphere $\mathbb{S}^2$. For example, dipoles in solution (Fig. 1 *C*, *ii*) can be represented by a constant-valued function $f^{(\text{solution})}(\hat{\mathbf{s}}_o) = C$, where C is constant, and the corresponding excited ODF (Fig. 1 *C*, *iii*) can be represented by $f^{(\text{excited})}(\hat{\mathbf{s}}_o) = C|\hat{\mathbf{s}}_o \cdot \hat{\mathbf{p}}|^2 = C\cos^2\theta$, where $\hat{\mathbf{p}}$ is the illumination polarization and θ is the angle between $\hat{\mathbf{s}}_o$ and $\hat{\mathbf{p}}$.

1.2. Polarized Dual-View Light-Sheet Microscopy Enables Selective Excitation, Selective Detection, and Reconstruction of Fluorescent Ensembles. In this section, we use ODFs as a tool to describe our imaging system, its contrast generation mechanisms, its limits, our reconstruction algorithms, and our visualizations.

Fig. 2*A* summarizes our dual-view excitation and detection strategy. Our core instrumentation (*SI Appendix*, section 2.1) consists of an asymmetric diSPIM frame equipped with a pair

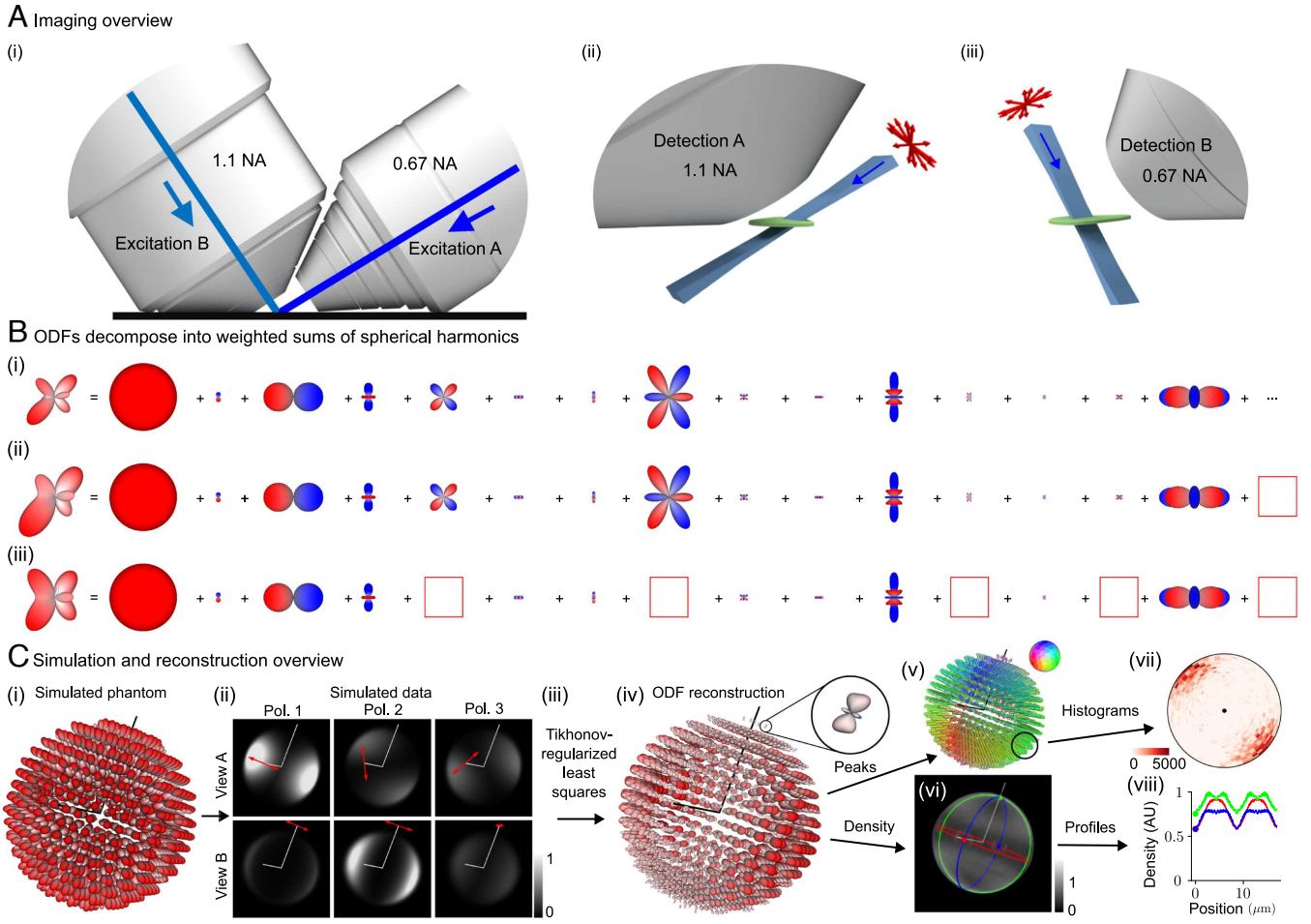

Fig. 2. Polarized dual-view inverted selective-plane illumination microscope (pol-diSPIM) data together with a physics-informed reconstruction enables volumetric measurement of three-dimensional orientation distribution functions. (*A*) (*i*) We imaged our samples with an asymmetric pair of objectives, each capable of excitation and detection. (*ii*) Illuminating our sample (green) with a light sheet (blue) from the 0.67 numerical aperture (NA) objective and detecting the emitted light from the 1.1 NA objective allows us to make planar measurements of diffraction-limited regions. Modulating the illumination polarization (red arrows) allows us to selectively excite ODFs within each diffraction-limited region, and orthogonal detection allows selective detection. (*iii*) Excitation from the 1.1 NA objective and detection from the 0.67 NA objective creates additional selective-excitation and selective-detection contrast and complementary spatial resolution. Scanning the sample through these polarized light sheets allows orientation-resolved volumetric acquisitions with more isotropic spatial resolution than detection from a single objective. (*B*) We used spherical harmonic decompositions of ODFs to simulate, reconstruct, and interpret our designs. (*i*) An example ODF is decomposed into the sum of an infinite number of spherical harmonics with the 15 smoothest nonzero terms shown. (*ii*) Truncating the infinite sum (red box at *Right*) smooths the ODF while preserving its overall shape, demonstrating the angular resolution our instrument can recover. (*iii*) Removing more terms (five red boxes) distorts the ODF and increases its symmetry, demonstrating the effect of missing components in the spatio-angular transfer function. (*C*) (*i*) A simulated phantom of radially oriented ODFs on the surface of a sphere is used to (*ii*) simulate a dataset. Each volume is simulated with a different illumination objective (rows) and illumination polarization (columns, red arrows indicate polarization, Pol. = Polarization), illustrating how selective excitation and detection (with optical axes indicated by white lines) results in contrast that encodes spatio-angular information. (*iii*) A physics-informed reconstruction algorithm allows us to recover (*iv*) ODFs in volumetric regions (*Inset*, a single ODF corresponding to a diffraction-limited volume). We reduce these reconstructions to lower-dimensional visualizations including (*v*) peak orientations, where the orientation and color of each cylinder indicates the direction along which most dipoles are oriented, and (*vi*) density, a scalar value indicating the total number of values within each voxel. We further summarize distributions of peak orientations with (*vii*) angular histograms, where the central dot indicates the viewing axis, and density with (*viii*) spatial profiles, where the colored profiles correspond to the circumferential profiles in (*vi*). Color bar labels refer to fractions of the maximum value.

of water immersion objectives, each capable of excitation and detection (32).

We use an excitation-path MEMS mirror (*SI Appendix*, section 2.2) to illuminate the sample with a light sheet from the 0.67 numerical aperture (NA) objective, detect the emitted light with the 1.1 NA objective, then scan the sample through the stationary light sheet to acquire an imaging volume. We repeat the acquisition with the objectives' roles swapped, illuminating with the 1.1 NA objective and detecting with the 0.67 NA objective.

We added a liquid crystal module to both excitation arms (*SI Appendix*, section 2.2), enabling our choice of arbitrary transverse polarization illumination. Instead of exploring all possible illumination polarizations, we restricted our possible choices to six linear polarization states, maximizing contrast while still enabling two-fold oversampling of the underlying signals (*SI Appendix*, section 3.1).

Our complete acquisition consists of a calibration procedure (*SI Appendix*, sections 4.2 and 8.2) and the following data acquisition loops from fastest to slowest (*SI Appendix*, section 4.3): (*xy*) camera frame, (*z*) stage scan positions, (v) views, (*p*) illumination polarization, (*c*) colors, and (*T*) time points. Our fastest single-time point, single-color acquisition consists of six volumes (three illumination polarizations per view) acquired within 3.6 s.

After deskewing (*SI Appendix*, section 5.1) and registering (*SI Appendix*, section 5.2) the raw data, we collect our irradiance

measurements into a single function $g_{p\mathrm{v}}(\mathfrak{r}_d)$, where p is a polarization index, v is a view index, and $\mathfrak{r}_d \in \mathbb{R}^3$ is a three-dimensional detector coordinate (*SI Appendix*, section 6.1). Next, we model the object that we are trying to estimate, a spatial distribution of ODFs, as a function $f(\mathfrak{r}_o, \hat{\mathbf{s}}_o)$, where $\mathfrak{r}_o \in \mathbb{R}^3$ is a three-dimensional object-space coordinate and $\hat{\mathbf{s}}_o \in \mathbb{S}^2$ is an orientation coordinate. Finally, we model the relationship between our data and our object as a shift-invariant integral transform

$$g_{p\mathrm{v}}(\mathfrak{r}_d) = \int_{\mathbb{R}^3} d\mathfrak{r}_o \int_{\mathbb{S}^2} d\hat{\mathbf{s}}_o \, h_{p\mathrm{v}}(\mathfrak{r}_d - \mathfrak{r}_o, \hat{\mathbf{s}}_o) f(\mathfrak{r}_o, \hat{\mathbf{s}}_o), \quad [1]$$

where $h_{p\mathrm{v}}(\mathfrak{r}_d - \mathfrak{r}_o, \hat{\mathbf{s}}_o)$ is a spatio-angular point-response function (compare with *SI Appendix*, section 6.8). The key features of Eq. **1** are 1) linearity: Doubling the number of fluorophore doubles the detected irradiance; 2) 3D spatial shift-invariance: A spatial shift of a fluorophore results in a spatial shift of its irradiance response; and 3) spatio-angular coupling: The spatial point-response function depends on the dipole orientation. In other words, $h_{p\mathrm{v}}(\mathfrak{r}_d - \mathfrak{r}_o, \hat{\mathbf{s}}_o)$ cannot be factored into a spatial part and an angular part. We assume that the thickness of the light sheet is approximately uniform over the field of view and that the detection-side point-response function is axially Gaussian over the width of the excitation light sheet, assumptions that we find to be true of our light sheets (further assumptions and details are provided in *SI Appendix*, sections 6.2–6.8).

Our goal is to estimate the spatial distribution of ODFs, $f(\mathfrak{r}_o, \hat{\mathbf{s}}_o)$, from the measured data, $g_{p\mathrm{v}}(\mathfrak{r}_d)$, but computing and inverting Eq. **1** is extremely computationally expensive. We reformulate Eq. **1** using spatio-angular transfer functions to simplify our computations and inversions with the additional benefit of improving our intuition about the imaging system's limits (*SI Appendix*, section 7). We apply spatial and spherical Fourier transforms to exploit the symmetries and bandlimits of Eq. **1** to rewrite it as

$$G_{p\mathrm{v}}(\mathfrak{v}) = \sum_{\ell=0,2,4} \sum_{m=-\ell}^{\ell} \mathsf{H}_{p\mathrm{v},\ell m}(\mathfrak{v}) \mathsf{F}_{\ell m}(\mathfrak{v}) \text{ for } |\mathfrak{v}_{\mathrm{v}}^{\perp}| < 2\mathrm{NA}_{\mathrm{v}}/\lambda, \quad [2]$$

where $G_{p\mathrm{v}}(\mathfrak{v}) = \mathcal{F}_{\mathbb{R}^3}\{g_{p\mathrm{v}}(\mathfrak{r})\}$ is the irradiance spectrum, the 3D spatial Fourier transform of the measured irradiance; $\mathsf{H}_{p\mathrm{v},\ell m}(\mathfrak{v}) = \mathcal{F}_{\mathbb{R}^3\times\mathbb{S}^2}\{h_{p\mathrm{v}}(\mathfrak{r}, \hat{\mathbf{s}}_o)\}$ is the dipole spatio-angular transfer function, the 3D spatial and spherical Fourier transform of the spatio-angular point response function; $\mathsf{F}_{\ell m}(\mathfrak{v}) = \mathcal{F}_{\mathbb{R}^3\times\mathbb{S}^2}\{f(\mathfrak{r}, \hat{\mathbf{s}}_o)\}$ is the sample's dipole spatio-angular spectrum; $\mathfrak{v} \in \mathbb{R}^3$ is a three-dimensional spatial-frequency coordinate; $\mathfrak{v}_{\mathrm{v}}^{\perp} \in \mathbb{R}^2$ is a two-dimensional transverse spatial-frequency coordinate for each view; ℓ is the spherical harmonic band index, interpretable as the sharpness of an angular component; m is the spherical harmonic intraband index, interpretable as the index over all orientation components at a specific angular sharpness ℓ; $\mathrm{NA}_A = 1.1$ and $\mathrm{NA}_B = 0.67$; and λ is the detection wavelength. The key features of Eq. **2** are 1) spatial band limits: Transverse spatial frequencies beyond $2\mathrm{NA}/\lambda$ are not detected; 2) angular discreteness: Instead of the continuous integral over the angular coordinate in Eq. **1**, the transfer function formulation uses a discrete sum over spherical harmonic coefficients; and 3) angular band limits: angular frequencies from the $\ell = 0, 2$, and 4 bands are the only terms transmitted. Fig. 2*B* demonstrates that an arbitrary ODF can be decomposed into a weighted sum of spherical harmonics, that a bandlimited version of an ODF is a smoother version of the original, and that missing intraband components can distort an ODF.

With an efficient forward model (Eq. **2**) in hand, we used simulations (Fig. 2 *C*, *i*, *ii*) to develop a Tikhonov-regularized least-squares reconstruction algorithm (Fig. 2 *C*, *iii*, *iv* and *SI Appendix*, sections 8.1 and 8.2). The spatio-angular coupling of the point-response function implies that we need to solve a small inverse problem for each spatial frequency—we cannot solve a small angular problem and subsequently solve a separate spatial problem. Therefore, our core algorithm consists of 1) applying a 3D spatial Fourier transform to the deskewed, registered, and calibrated volumes, 2) collecting the Fourier coefficients from each polarization and view into a 6×1 vector, one vector for each spatial frequency, then 3) multiplying each vector by a precomputed spatial-frequency-specific 15×6 matrix before 4) applying an inverse 3D Fourier transform and storing the result: a set of 15 spherical harmonic coefficient estimates for each spatial point (*SI Appendix*, section 8.3 and Table S4).

We found that directly visualizing the complete reconstruction, a 3D spatial distribution of ODFs (Fig. 2 *C*, *iv*) provided the most information about the sample but was visually overwhelming for most applications. We developed several tools for reducing the visual complexity of the reconstructions (*SI Appendix*, sections 8.4 and 8.5) including peak-cylinder visualizations where the color and orientation of each cylinder encodes the axis along which most dipoles are oriented (Fig. 2 *C*, *v*), histogram visualizations showing peak orientations in larger regions (Fig. 2 *C*, *vii*), and scalar metrics including density, proportional to the number of dipoles in each region (Fig. 2 *C*, *vi*, *viii*) and generalized fractional anisotropy (GFA) (33).

1.3. Light-Sheet Tilting Enables Recovery of All Three-Dimensional Orientations. The angular band limit of our transfer function (Eq. **2**) deserves additional interpretation. Selective excitation with linearly polarized light will generate excited ODFs of the form $\cos^2\theta$ multiplied by the object ODF, which means that angular components of degree two, the $\ell = 2$ spherical harmonics, from the object ODF can be encoded into detected irradiances. Similarly, selective detection will generate irradiance patterns of the form $C_1 + C_2 \sin^2\phi$ multiplied by the excited ODF (the constants C_1 and C_2 are due to the finite detection numerical aperture), meaning that selective excitation can encode the angular components of degree zero and two, the $\ell = 0$ and $\ell = 2$ spherical harmonics. When we combine selective excitation and detection, the imaging system can encode the $\ell = 0, 2$ and 4 components of the object ODF into the measured irradiance patterns. Similar to spatial structured illumination microscopy (SIM), angularly structured (polarized) illumination aliases high angular frequency components into the detection pass band. Additionally, only even ℓ terms are transmitted—antipodally symmetric ODFs mean that ODFs consist of only even-ℓ terms.

This argument led us to expect that we could recover all orientations from our sample by exploiting selective excitation and detection, using oversampled illumination polarizations if necessary. We found our intuition to be incorrect, finding that no number of illumination polarizations was enough to recover all orientations from our imaging system. A close inspection of our angular transfer function revealed that we did not properly consider intraband angular holes.

Fig. 3*A* shows all fifteen $\ell = 0, 2$ and 4 spherical harmonics along with the four intraband angular holes in our transfer

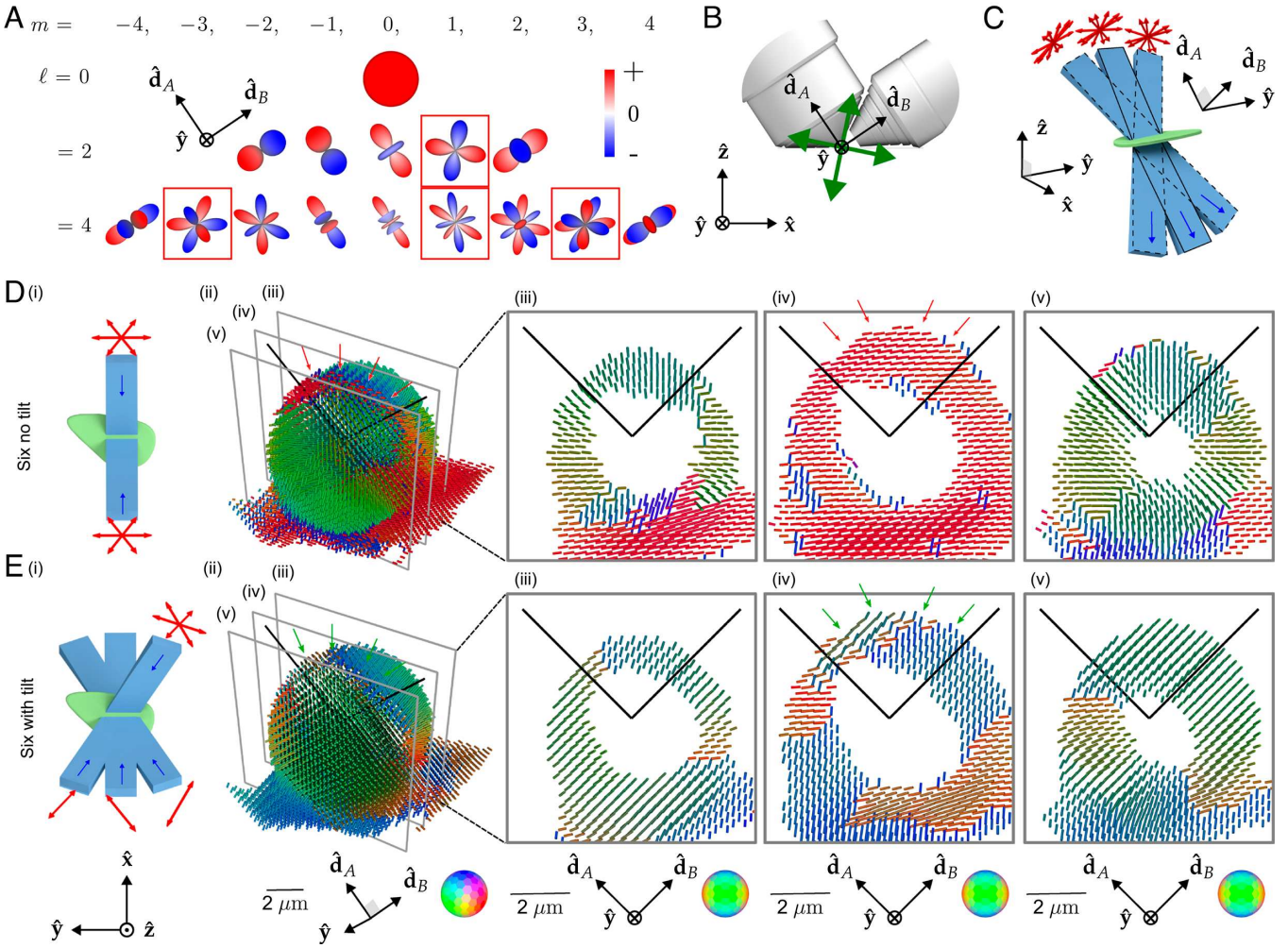

Fig. 3. Light-sheet tilting enables experimental recovery of second-order spherical harmonic coefficients and all peak orientations. (*A*) We found that our spatio-angular transfer function had "angular holes" when expressed in a basis of spherical harmonics aligned with the detection axes. Red boxes indicate null functions, spherical harmonics that are not passed to the detected data. (*B*) These angular holes correspond to the ambiguity between dipoles that bisect the optical axes of the two objectives (green arrows). Dipoles that are oriented along these two directions will be identically excited, giving rise to signals that cannot distinguish these orientations. (*C*) We added MEMS mirrors to each excitation arm, enabling light-sheet illumination in the typical straight-through configuration (blue rectangle with solid outline) and the new tilted configurations (blue rectangles with dashed outlines). Tilting the light sheet makes new polarization orientations (red arrows) accessible while illuminating the same positions in the sample. (*D*) (*i*) A schematic of our **Six no tilt** acquisition scheme, where the sample (green) is illuminated with light sheets (light blue) propagating parallel to the optical axes of the objectives (dark blue arrows) under three different polarization illuminations per light sheet (red arrows). (*ii*) Peak cylinder reconstruction from experimental data acquired from a giant-unilamellar vesicle (GUV), where color and orientation encodes the most frequent dipole orientation from within each voxel, spaced by 260 nm. We expect the dipole orientations to be everywhere normal to the GUV, but instead see a red stripe across the top of the reconstructed GUV (see red arrows). (*iii–v*) Slices through the peak cylinder reconstruction, with incorrect orientations marked with red arrows. (*E*) (*i*) A schematic of our **Six with tilt** acquisition scheme, which uses a view-asymmetric combination of polarization and tilted light sheets to acquire more angular information from six illumination samples. (*ii–v*) Peak cylinder reconstruction using tilted light sheets shows recovery of all peak orientations [see green arrows in (*ii*) and (*iv*)]. Each column of (*D* and *E*) uses a single coordinate system described below the column where $\hat{\mathbf{d}}_A$ and $\hat{\mathbf{d}}_B$ are the detection optical axes.

function. Mathematically, the spherical harmonic functions are grouped into $(2\ell+1)$-dimensional bands that form rotationally invariant subspaces of the spherical functions, so if a single member of a band is missing we cannot expect rotationally invariant angular resolution. The $\ell = 2$ and $m = 1$ spherical harmonic is a particularly consequential angular hole because it is the single missing member of the lowest nonzero-order $\ell = 2$ band, implying that there are some orientations that we cannot recover. The angular hole corresponds to an ambiguity between dipoles that bisect the optical axes, as shown in Fig. 3*B*. The angular hole corresponds to a >10-fold smaller transmitted amplitude than other coefficients, which means that this component is easily corrupted by noise during imaging. Our best attempts to estimate the $\ell = 2$ and $m = 1$ spherical harmonic failed due to poor SNR caused by poor transmission.

We asked what a minimally modified version of our imaging system without an $\ell = 2$ angular hole would look like, and we used the ambiguity described above to propose that light-sheet tilting (Fig. 3*C* and *SI Appendix*, section 3.2 and Figs. S2 and S3), enabled by a micro-electromechanical systems (MEMS) mirror placed conjugate to the illumination pupil, would allow us to fill the angular hole in the transfer function while illuminating the same spatial region.

We need to make at least 6 tilting polarization-diverse measurements to recover components from all members of the $\ell = 0$ and 2 bands. We simulated transfer functions and optimized the condition number of our sampling schemes,

searching through ~2×10^6 possible sampling schemes to settle on the schemes depicted in Fig. 3 *D* and *E*, *i*. *SI Appendix*, sections 3 and 9 provide more detail about our sampling choices.

Although we measure some components from the $\ell = 0$, 2, and 4 bands, we do not recover all of their components. Our imaging system can access all orientations by recovering components from all members of the $\ell = 2$ band. Recovering the $\ell = 4$ band would enable better angular resolution, but it would not enable access to more orientations than the $\ell = 2$ band. Notably, our system can recover a component of the $\ell = 0$ band (corresponding to isotropic ODFs), but it fails to recover it completely. While our system is not uniformly sensitive to all orientations and cannot recover isotropic ODFs, it can recover peak orientations in all 3D directions.

Fig. 3 *D* and *E* compare a peak-cylinder reconstruction of a GUV with and without light-sheet tilting. The GUV is labeled with FM1-43, a membrane-crossing dye with a dipole transition moment oriented normal to the membrane (34), so we expect a pin-cushion-like reconstruction. Fig. 3 *D*, *ii*, *iv* show incorrect peak cylinder orientations in areas marked with red arrows—peak cylinders lie flat on the surface of the GUV when they should point radially outward. Fig. 3 *E*, *ii*, *iv* show that light-sheet tilting corrects the problem, with continuously radial peak cylinders across the surface of the GUV, highlighted in regions with green arrows. All subsequent data and reconstructions are performed with light-sheet tilting.

1.4. pol-diSPIM Measurements of Fixed Samples Validate and Extend Our Knowledge of Oriented Biological Structures. Having demonstrated that light-sheet tilting enables recovery of all orientations in GUVs, we proceeded to validate and apply our method to other three-dimensional samples (Fig. 4 and Movies 1–6) including GUV, xylem, and actin samples. Fig. 4*A* shows ODF, peaks, density, and radial profile views of the FM1-43-labeled GUV from Fig. 3. While the peak-cylinder visualization (Fig. 4 *A*, *ii*) is the easiest-to-interpret reconstruction, the ODF reconstruction can reveal the subtlest changes that our system can measure, e.g. two different ODFs can have identical peak cylinders. The density reconstruction (Fig. 4 *A*, *iii* and Movies 1 and 2) gives a view that is familiar to fluorescence microscopists, with brightness encoding the density. Finally, we measure radial profiles (Fig. 4 *A*, iv) of the density (Fig. 4 *A*, *v*) indicating that the fluorophores are most dense near the GUV's surface with two-fold variation in intensity due to the nonuniform

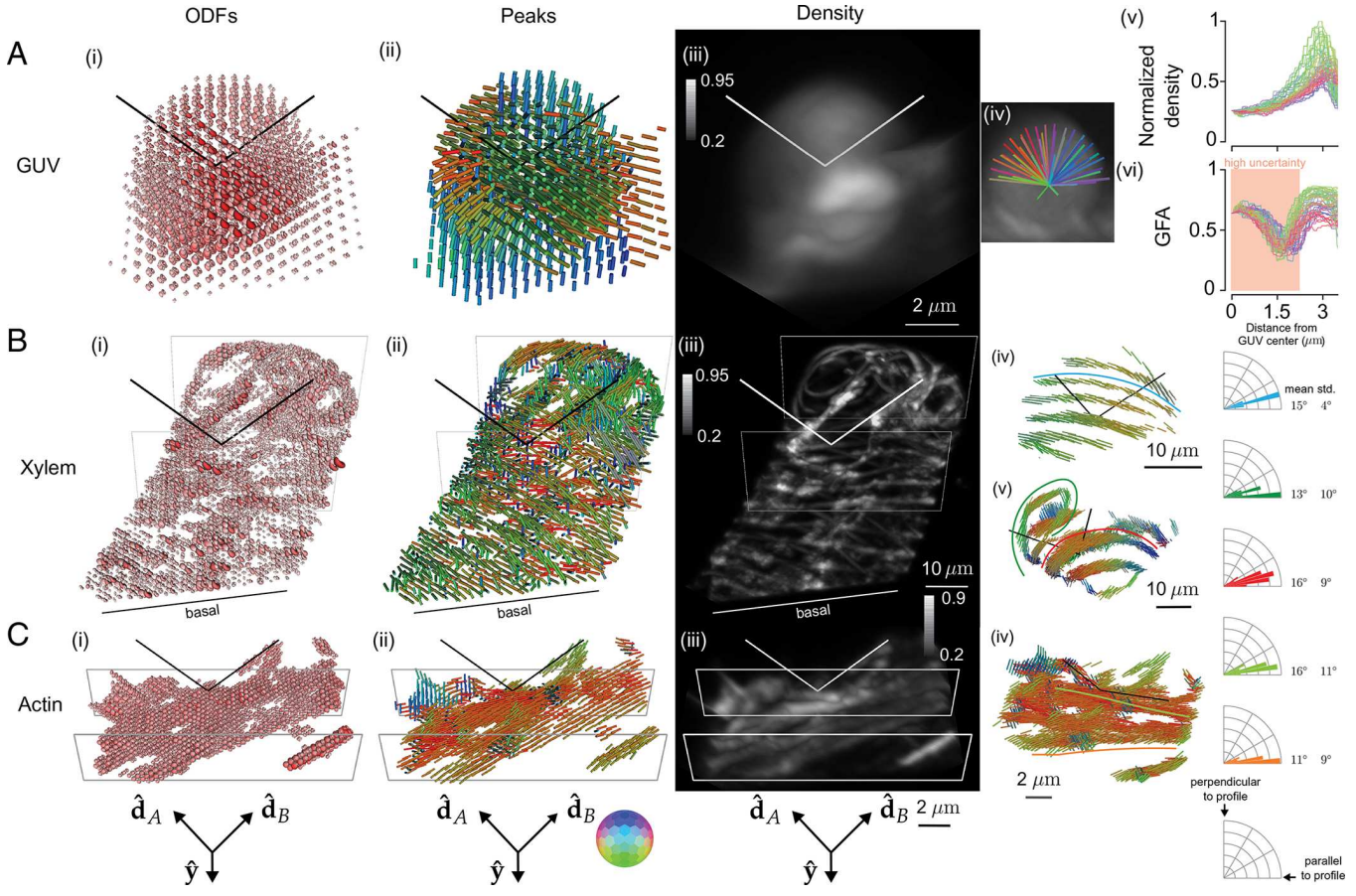

Fig. 4. Reconstruction of GUV, xylem, and actin samples validate pol-diSPIM's accuracy and extend known 2D orientation results to 3D. (*A*) A ~6 μm-diameter GUV labeled with FM1-43 with (*i*) ODFs and (*ii*) peak cylinders separated by 650 nm. Radial profiles through the density map (*iv*) are used to plot density (*v* and *vi*) generalized fractional anisotropy (GFA) as a function of distance from the center of the GUV. In regions with low density, the GFA is dominated by noise and background contributions, so we have marked these regions as "high uncertainty" (red background). (*B*) A xylem cell with its cellulose labeled by fast scarlet with (*i*) ODFs and (*ii*) peak cylinders separated by 1.56 μm. ROIs (*iv* and *v*) show peak cylinders separated by 650 nm with overlaid profiles (blue, green, red lines) that pass through the center of their nearest fibers (see *SI Appendix*, Fig. S17 for profiles through density), with histograms (blue, green, and red correspond to profiles) showing recovered orientations that run parallel to their fibers within ~15 degrees. (*C*) U2OS cells with actin labeled by phalloidin 488 with (*i*) ODFs and (*ii*) peak cylinders separated by 390 nm. (*v*) A different view of peak cylinders with overlaid profiles (light green, orange lines) that pass through the center of their nearest fibers (see *SI Appendix*, Fig. S19 for profiles through density), with histograms (light green and orange correspond to profiles) showing recovered orientations that run parallel to their fibers within ~10 degrees. Each column's camera orientation and orientation-to-color map is displayed in the *Bottom* row. See also, Movies 1–6. Color bar labels refer to fractions of the maximum value.

spatial transfer function of our imaging system—although the transfer function is nonzero for the second-order harmonics, it remains nonuniform. We also measure radial profiles of the GFA (Fig. 4 *A*, *vi*), a scalar measure with GFA = 1 indicating a strongly anisotropic structure and GFA = 0 indicating an isotropic structure. The GFA profiles show similar behavior for all orientations, starting at ∼0.6 near the GUV's center, dipping to ∼0.25, then reaching peaks of ∼0.75 at the GUV's surface before dropping again. The behavior near the peak can be interpreted as the increase in oriented structures compared to the random orientations nearby, but the high GFA value in the center of the GUV indicates the effects of noise in low-density regions. We consistently observed experiment-to-experiment variation in the value of GFA and orientations in background regions, leading us to only draw conclusions from GFA and peaks in regions with a density above a background threshold; see *SI Appendix*, section 10 for comparison with simulation (*SI Appendix*, Fig. S14) and more detailed analysis (*SI Appendix*, Fig. S15).

Fig. 4*B* shows fast-scarlet labeled cellulose in a xylem cell (Movies 3 and 4 and *SI Appendix*, Figs. S16 and S17), showing dipole orientations parallel to the long axis of the cellulose fibers as expected from 2D studies (35). We observe 3D orientations tracking the cellulose fibers as they curve in space (peaks parallel to fiber long axes within 12 to 16 degrees, *SI Appendix*, Fig. S17), spatially disorganized orientation regions on the basal surface near the coverslip, and the ability to distinguish cellulose fibers that were indistinguishable on the basis of their merged density, but exhibited distinct orientations (Fig. 4 *B*, *v*). The disorganization on the basal side is consistent with damage caused by air drying during sample preparation. The thinness of the windings likely indicates a cell in the early stages of differentiation, which would make these cells particularly susceptible to damage via air drying.

Fig. 4*C* shows Alexa Fluor 488 phalloidin-labeled actin in a U2OS cell (Movies 5 and 6 and *SI Appendix*, Figs. S16, S19, and S20), showing dipole orientations parallel to the long axis of the actin filaments as expected (22) (peaks parallel to fiber long axes within 5 to 17 degrees, Fig. 4 *C*, *iv*). We observe distinct actin filaments, some lying flat in the plane of the coverslip while others reach off the coverslip oriented nearly normal to its surface, *SI Appendix*, Fig. S16*B*.

1.5. pol-diSPIM Measurements of Cells Grown on Nanowires Show Local-Global Alignment Correlations. Having validated our system's ability to measure 3D orientations in actin, we used our system to study actin orientations with respect to fixed landmarks by imaging phalloidin-labeled 3T3 mouse fibroblasts grown on nanowire arrays (Figs. 5 and 6), a model system for studying cell migration.

Cells' immediate environment, the extracellular matrix (ECM), is fibrous, consisting of individual fibrils and bundled fibers ranging in diameter from a few hundred nanometers to several micrometers (36–38), organized in a diverse range of fiber densities, pore sizes, and network architectures, including aligned (39) and crossed-fiber arrangements (40–43). The complexity of studying cell migration in 3D motivated studies with simpler 1D substrates, which were found to replicate many of the features of 3D matrices while differing from observations on conventional 2D culture systems (44). Further, in fibrous environments with large pore sizes, cells contact only a few fibers, signifying that cells in vivo can be suspended (45–48) and that imaging cells suspended on 1D and 2D wire arrays can provide biological insight.

Previously, we showed that cellular shapes can be tuned to the underlying fiber network, with actin stress fibers aligning along ECM-fibers in cells attached to single and multiple parallel fibers, and intersecting actin networks in cells attached to a crosshatch network of fibers (49, 50). In a subsequent study, the underlying actin networks were found to regulate mitotic outcomes through actin retraction fibers connecting the rounded mitotic cell body to interphase adhesion sites (51). In both studies, while the patterning of actin networks matched the arrangement of underlying ECM networks, it was unclear how far the effect of adhesions on fibers was extended to shape the actin networks.

Here, we used pol-diSPIM imaging to investigate long-range adhesion effects in 3D. We deposited suspended fibers ∼200 nm in diameter, imaged phalloidin-labeled 3T3 mouse fibroblasts grown on these nanowire arrays, and measured the local orientation of actin networks. We imaged in two channels, a 488 nm channel for BDP FL Maleimide dye wire annotations, and a 561 nm channel for Alexa Fluor 568 phalloidin orientation measurements (*SI Appendix*, section 5.3).

Fig. 5*A* shows a density reconstruction of a single cell with region of interests (ROIs) highlighted for closer inspection. The peak cylinders (Fig. 5*B*) indicate that actin filaments and the dipoles that label them coalign with their nearest nanowires, and the histograms (Fig. 5*C*) show distinct in-plane and out-of-plane filament populations from within each ROI, including out-of-plane populations that would be invisible to traditional anisotropy measurements. Additionally, we observe more disorder and larger out-of-plane populations for ROIs near the center of the cell (Fig. 5 *B* and *C*, *ii*, *iv*) than regions near nanowires (Fig. 5 *B* and *C*, *i*, *iii*, *v*).

To evaluate dipole orientations of F-actin with respect to their nearest wires, we developed a pair of scalar metrics, parallelism, and radiality (*SI Appendix*, section 8.6), and computed maps of these metrics in regions with a total number of counts across polarizations and views greater than 5,000, a threshold that rejects background regions.

We used these metrics to further investigate nine field of views (FOVs), with three FOVs for each of three different nanowire arrangements: single, paired, and crossed nanowires (Fig. 6*A*). Across each FOV we calculated parallelism and radiality for voxels <5 μm from their nearest wire, and we compared these metrics between FOVs and wire arrangements (Fig. 6*B*). We found the FOVs with the same wire arrangement clustered at distinct parallelism and radiality values and showed no significant differences (colors in Fig. 6*C*), while FOVs with different wire arrangement showed significantly different values for parallelism and radiality. The crossed wire arrangement showed significantly lower parallelism (0.70 ± 0.24, mean ± SD across voxels) than single (0.88 ± 0.11) and paired (0.89 ± 0.11) arrangements, indicating local-scale disorder of actin filaments created by the presence of wires in multiple orientations. Consistent with this observation, cells on crossed wires showed significantly increased radiality (0.51 ± 0.28) over cells on single wires (0.17 ± 0.13). Fig. 5*v* shows an ROI consistent with these broader conclusions, where peaks show increased disorder near a wire crossing. Further, we found that parallelism decreases as a function of distance from each voxel's nearest wire (*SI Appendix*, Fig. S21), and for the crossed wire condition, we found more parallelism near thin wires than thick wires (*SI Appendix*, Fig. S22).

Further, we calculated each FOV's aspect ratio, a global measure of the effect of nanowire topology on cell polarization, and found that the aspect ratio was positively and negatively correlated with parallelism ($r = 0.66$) and radiality ($r = -0.78$), respectively. Both of these correlations are interpretable as evidence of a quantitative relationship between local 3D orientation of F-actin within actin bundles and global cellular

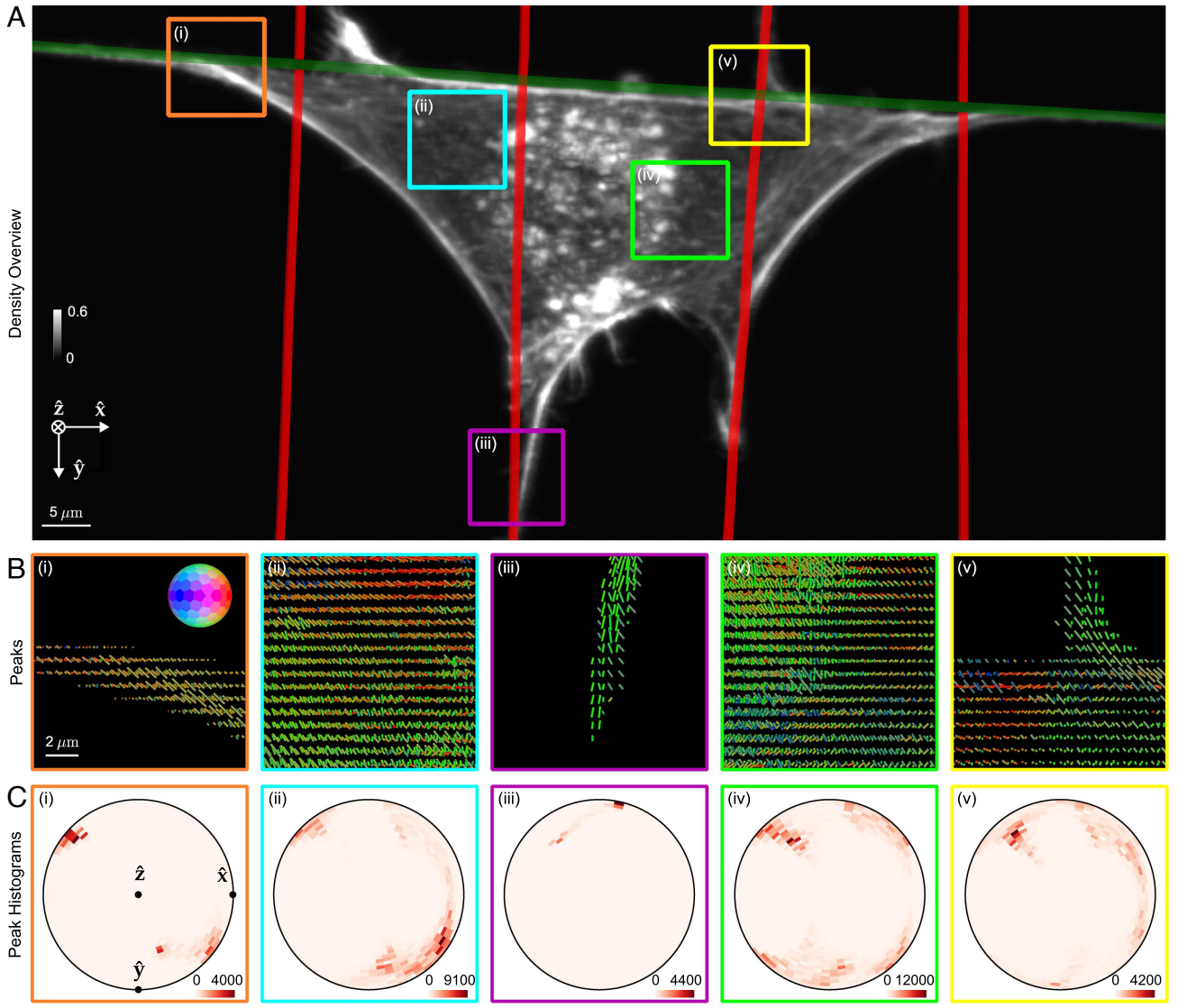

Fig. 5. pol-diSPIM measurements of phalloidin-labeled 3T3 mouse fibroblasts grown on nanowires show dipoles oriented parallel to their nearest nanowires and reveal distinct out-of-plane dipole populations across the cell. (*A*) Reconstructed density maximum intensity projection of a cell grown on crossed nanowires, with hand-annotated wires measured from a wire-specific channel highlighted with red and green lines. ROIs (*i–v*) are outlined in color and examined in subsequent panels. Color bar labels refer to fractions of the maximum value. (*B*) Peak cylinders drawn every 780 nm in regions with total counts > 5,000, colored by orientation (see *Inset* color hemisphere), with lengths proportional to the maximum diameter of the corresponding ODF. (*C*) Histogram of all peak cylinders with total counts > 5,000 in each ROI. Bins near the edge of the circle indicate in-plane orientations, bins near the center indicate out-of-plane orientations, and dots mark the Cartesian axes on the histogram.

response to changes in extracellular matrix substrates and its organization.

Taken together, our measurements demonstrate that the effect of an oriented and anisotropic ECM network on 3D orientational order is felt over cell-scale distances, and topographical intersections, which mimic more isotropic ECM, diminish local F-actin order. Our findings are consistent with previous studies of 2D actin filament orientation and cell shape (52), and we are excited by our system's ability to extend these findings to 3D.

2. Discussion

This work develops a theoretical and experimental bridge between 2D anisotropy measurements and 3D single-molecule orientation measurements. ODFs and the spatio-angular transfer function formalism helped us identify the limits of our imaging system, and we used theory to improve our design with light-sheet tilting. A similar light-sheet tilting scheme was used to reduce absorptive-streaking artifacts (53), but here we use tilting to increase the angular diversity of polarized illumination, allowing us to recover all orientations to extend and draw conclusions about oriented fluorescent samples in 3D. We note that light-sheet tilting is not the only solution to all-orientation imaging—we can imagine many combinations of calibrated illumination and detection aberrations that could reveal all orientations—but it is a practical approach that we pursued here.

Spatio-angular transfer functions point us toward further improvements. Designs that use polarization splitting to make simultaneous selective-detection measurements will give access to the $\ell = 4$ band without trading off speed, and designs that have a more uniform angular response than our system will improve on our ability to draw conclusions from samples in all orientations. Polarized two-photon excitation and emission (54) provide $\cos^4\theta$-behavior, sharper than the single-photon

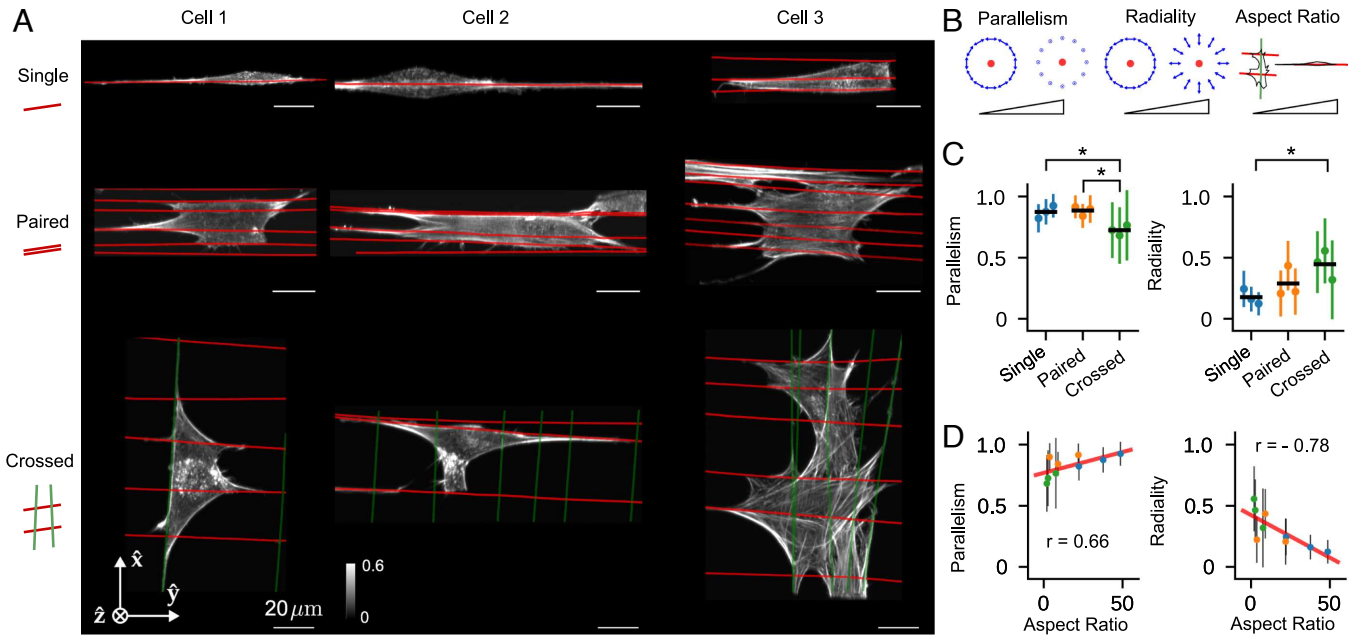

Fig. 6. Measurements of 3T3 mouse fibroblasts grown on different nanowire arrangements show correlations between voxel-scale 3D orientational order of F-actin and cell-scale orientations. (*A*) Reconstructed density maximum intensity projections of three cell repeats (columns) grown on varying nanowire arrangements (rows) named "Single," "Paired," and "Crossed" (cartoons at *Left*). Wires are overlaid as red and green lines. Color bar labels refer to fractions of the maximum value. (*B*) We collected reconstructed peak directions in voxels that were <5 μm from a wire and had total counts > 5,000, calculated their parallelism and radiality with respect to their nearest wire (see *Inset* cartoons where the red dot indicates a wire, and blue arrows indicate the neighboring peak directions for strongly parallel and radial peaks), and plotted their mean (dots) and SD (error bars) for each cell and nanowire arrangement (colors). Additionally, we calculated each cell's "Aspect Ratio," the ratio of the largest and smallest eigenvalues of the cell's moment of inertia tensor (with the reconstructed density as a proxy for mass). (*C*) We compared population means (horizontal black lines) with a *t*-test and marked $P < 0.05$–significant differences with asterisks. (*D*) We compared our local voxel-wise parallelism and radiality metrics to the cell's global aspect ratio. We found positive and negative correlations between the aspect ratio and the parallelism and radiality, respectively, indicating local-global correlations in cellular behavior. Colored dots match (*C*), the red line is a linear fit to all nine data points, and the annotated *r* values are Pearson correlation coefficients.

$\cos^2\theta$-behavior considered here, leading to potential for accessing the $\ell = 6$ and 8 bands.

While single-molecule experiments surpass our system's spatio-angular precision [e.g. Zhang et al. (21) report spatial precision of 10.9 nm and angular precision of 2 degrees compared to our system's spatial resolution of $\lambda/(2\text{NA}) = 500\ \text{nm}/(2 \times 1.1) = 227$ nm and angular performance of >80% of peak orientations within a cone of 42-degree half angle; see *SI Appendix*, section 11], our system excels in throughput (3.6 s per volume, $\sim 150 \times 160 \times 50\ \mu\text{m}^3$) and SNR. For these reasons, we view single-molecule and ensemble orientation techniques as complementary techniques.

Imaging speed limits our ability to draw conclusions from living cells. We measure orientation signals via serial polarized illumination measurements taken over a few seconds, so translational motion on this timescale is indistinguishable from an oriented sample. Although we made many measurements of living cells with our system, we decided to withhold these data from publication as the possibility of spatial motion repeatedly called our conclusions into question. Replacing our polarized illumination strategy with a detection-side polarization splitting strategy provides one path for speed improvement.

We were constrained by a limited palette of fluorescent reporters that rigidly attach to biological structures. Although we are encouraged by recent developments of genetically encoded actin orientation probes (55), we see room for development of bright oriented probes across the spectrum in more biological structures. We see probes as the major limitation in this field, not instrumentation.

Here, we made steady-state measurements, considering only quasi-static fluorescent reporters. Time-resolved orientation measurements provide a large set of possibilities for this field (56, 57), and combining time-resolved measurements with reversibly switchable proteins allows measurement of a wide range of reorientation timescales (58), giving access to reorientation timescales of large protein complexes. We are excited for future developments that probe long-timescale reorientation of fluorophores trapped in 3D angular potentials.

While we have assumed that excitation and emission dipoles moments are parallel, some fluorophores have >20° angles between these moments (31, 59). Characterizing the complete orientation distribution of an ensemble of molecules with misaligned dipole moments would require an extended version of the ODF beyond the spherical distributions discussed here to distributions over SO(3). Extensions in theory, measurement, reconstruction, and visualization are needed before pursuing this direction.

Fluorescence anisotropy can be used for homoFRET measurements of molecular binding (60), and an early nontilting variant of the system described here was used to make such measurements (61). We hope that future efforts will encode additional physical parameters, such as force and voltage, into the orientation and rotational mobility of fluorescent probes with readouts enabled by systems like the one described here.

3. Materials and Methods

SI Appendix, section 12 describes sample-preparation protocols for beads, calibration slides, giant unilamellar vesicles, actin, xylem, and fiber-network samples. *SI Appendix*, section 2 describes our imaging instrumentation, a polarized dual-view light-sheet system. *SI Appendix*, sections 3–11 describe

our image processing algorithms, which consist of deskewing, registration, deconvolution, and visualization. Raw and processed data are available on the BioImage Archive (S-BIAD1055). Preprocessing analysis software is available at https://github.com/eguomin/microImageLib. Reconstruction and visualization software is available at https://github.com/talonchandler/polaris.

Data, Materials, and Software Availability. Multidimensional images, preprocessing analysis software, and reconstruction and visualization software data have been deposited in BioImage Archive (https://www.ebi.ac.uk/biostudies/bioimages/studies/S-BIAD1055) (62) and GitHub (https://github.com/eguomin/microImageLib (63); https://github.com/talonchandler/polaris (64)).

ACKNOWLEDGMENTS. We thank Applied Scientific Instrumentation for sharing drawings and assisting with hardware. This research was supported by the intramural research programs of the National Institute of Biomedical Imaging and Bioengineering, NIH. We thank the Marine Biological Laboratory (MBL), for providing a meeting and brainstorming platform. T.C. was supported by a University of Chicago Biological Sciences Division Graduate Fellowship and an O'Brien-Hasten Research Collaboration Award. H.S. and P.J.L.R. acknowledge the Whitman Fellows program at MBL for providing funding and space for discussions valuable to this work. P.J.L.R. acknowledges funding from the NIH under grant no. R01EB026300. This research is funded in part by the Gordon and Betty Moore Foundation. This work was supported by the HHMI and the Janelia Visiting Scientists Program. This article is subject to HHMI's Open Access to Publications policy. HHMI lab heads have previously granted a nonexclusive CC BY 4.0 license to the public and a sublicensable license to HHMI in their research articles. Pursuant to those licenses, the author-accepted manuscript of this article can be made freely available under a CC BY 4.0 license immediately upon publication. A.K. would like to acknowledge funding from the Chan Zuckerberg Initiative through Imaging Scientist Program and the Arnold and Mabel Beckman Foundation for the lightsheet award. Work in the Baskin laboratory on cellulose is supported by the Division of Chemical Sciences, Geosciences, and Biosciences, Office of Basic Energy Sciences of the U.S. Department of Energy under grant no. DE-FG-03ER15421. R.O. gratefully acknowledges funding from the NIH/NIGMS under grant no. R35GM131843 and from the Marine Biological Laboratory through the Inoué Endowment Fund. A.S.N. acknowledges partial funding from the NSF (Grants No. 1762468, 2119949, and 2422340) and the NIH (1R01 HL162822-01A1). A.S.N. acknowledges the Institute of Critical Technologies and Science and Macromolecules Innovative Institute at Virginia Tech for supporting this study. H.L. acknowledges funding from the National Natural Science Foundation of China under grant no. 62427807; M.G. acknowledges funding from the National Natural Science Foundation of China under grant no. 62475232; J.L. acknowledges the support from Zhejiang University Global Partnership Fund.

Author affiliations: [a]Chan Zuckerberg Biohub San Francisco, San Francisco, CA 94158; [b]Department of Radiology, University of Chicago, Chicago, IL 60637; [c]State Key Laboratory of Extreme Photonics and Instrumentation, College of Optical Science and Engineering, Zhejiang University, Hangzhou, Zhejiang 310027, China; [d]Laboratory of High Resolution Optical Imaging, National Institute of Biomedical Imaging and Bioengineering, NIH, Bethesda, MD 20892; [e]Advanced Imaging and Microscopy Resource, NIH, Bethesda, MD 20892; [f]HHMI, Janelia Research Campus, Ashburn, VA 20147; [g]Department of Mechanical Engineering, Virginia Tech, Blacksburg, VA 24061; [h]Cell Biology and Physiology Center, National Heart, Lung, and Blood Institute, NIH, Bethesda, MD 20892; [i]Bell Center, Marine Biological Laboratory, Woods Hole, MA 02543; [j]Department of Biology, University of Massachusetts, Amherst, MA 01003; [k]Whitman Center, Marine Biological Laboratory, Woods Hole, MA 02543; [l]Department of Molecular Biology and Biochemistry, Simon Fraser University, Burnaby, BC V5A 1S6, Canada; [m]Department of Clinical Sciences, Lund University, Lund, Scania SE-221 00, Sweden; and [n]Wallenberg Centre for Molecular Medicine, Lund University, Lund, Scania SE-221 00, Sweden

Author contributions: T.C., M.G., R.S.F., S.B.M., A.K., V.S., A.S.N., R.O., P.J.L.R., and H.S. designed research; T.C., M.G., Y.W., A.A., R.S.F., S.B.M., A.K., V.S., A.S.N., R.O., P.J.L.R., and H.S. performed research; T.C., M.G., Y.S., J.C., Y.W., A.A., S.B.M., A.K., T.I.B., V.J., R.O., P.J.L.R., and H.S. contributed new reagents/analytic tools; T.C., M.G., Y.W., J.L., A.A., R.S.F., T.I.B., H.L., V.S., A.S.N., R.O., P.J.L.R., and H.S. analyzed data; T.C. drafted the paper, figures, and supplements; P.J.L.R. and H.S. oversaw the work; and T.C., M.G., P.J.L.R., and H.S. wrote the paper.

Competing interest statement: T.C., Y.W., S.B.M., A.K., R.O., P.J.L.R., and H.S. hold US Patent #11428632.

1. S. Brasselet, M. A. Alonso, Polarization microscopy: From ensemble structural imaging to single-molecule 3D orientation and localization microscopy. *Optica* **10**, 1486–1510 (2023).
2. J. R. Lakowicz, *Principles of Fluorescence Spectroscopy* (Springer, New York, ed. 3, 2006).
3. D. M. Jameson, J. A. Ross, Fluorescence polarization/anisotropy in diagnostics and imaging. *Chem. Rev.* **110**, 2685–2708 (2010).
4. D. Axelrod, Carbocyanine dye orientation in red cell membrane studied by microscopic fluorescence polarization. *Biophys. J.* **26**, 557–573 (1979).
5. P. Ferrand *et al.*, Ultimate use of two-photon fluorescence microscopy to map orientational behavior of fluorophores. *Biophys. J.* **106**, 2330–2339 (2014).
6. A. M. Vrabioiu, T. J. Mitchison, Structural insights into yeast septin organization from polarized fluorescence microscopy. *Nature* **443**, 466–469 (2006).
7. B. S. DeMay, N. Noda, A. S. Gladfelter, R. Oldenbourg, Rapid and quantitative imaging of excitation polarized fluorescence reveals ordered septin dynamics in live yeast. *Biophys. J.* **101**, 985–994 (2011).
8. M. McQuilken *et al.*, Analysis of septin reorganization at cytokinesis using polarized fluorescence microscopy. *Front. Cell. Dev. Biol.* **5**, 42 (2017).
9. M. Kampmann, C. E. Atkinson, A. L. Mattheyses, S. M. Simon, Mapping the orientation of nuclear pore proteins in living cells with polarized fluorescence microscopy. *Nat. Struct. Mol. Biol.* **18**, 643–649 (2011).
10. J. M. Brockman *et al.*, Mapping the 3D orientation of piconewton integrin traction forces. *Nat. Methods* **15**, 115–118 (2017).
11. A. T. Blanchard, J. Brockman, K. Salaita, A. L. Mattheyses, Variable incidence angle linear dichroism (VALiD): A technique for unique 3D orientation measurement of fluorescent ensembles. *Opt. Express* **28**, 10039–10061 (2020).
12. I. I. Smalyukh, S. V. Shiyanovskii, O. D. Lavrentovich, Three-dimensional imaging of orientational order by fluorescence confocal polarizing microscopy. *Chem. Phys. Lett.* **336**, 88–96 (2001).
13. T. Ohzono, K. Katoh, J. Fukuda, Fluorescence microscopy reveals molecular localisation at line defects in nematic liquid crystals. *Sci. Rep.* **6**, 1–9 (2016).
14. K. Zhanghao *et al.*, Super-resolution imaging of fluorescent dipoles via polarized structured illumination microscopy. *Nat. Commun.* **10**, 1–10 (2019).
15. M. Guan *et al.*, Polarization modulation with optical lock-in detection reveals universal fluorescence anisotropy of subcellular structures in live cells. *Light Sci. Appl.* **11**, 1–13 (2022).
16. S. Zhong *et al.*, Three-dimensional dipole orientation mapping with high temporal-spatial resolution using polarization modulation. *PhotoniX* **5**, 12 (2024).
17. T. Wu, M. R. King, M. Farag, R. V. Pappu, M. D. Lew, Mapping inhomogeneous network structures within biomolecular condensate using single-molecule imaging and tracking of fluorogenic probes. *Biophys. J.* **122**, 296a (2023).
18. A. S. Backer *et al.*, Single-molecule polarization microscopy of DNA intercalators sheds light on the structure of S-DNA. *Sci. Adv.* **5**, eaav1083 (2019).
19. T. Ding *et al.*, Single-molecule orientation localization microscopy for resolving structural heterogeneities between amyloid fibrils. *Optica* **7**, 602–607 (2020).
20. J. F. Beausang, D. Y. Shroder, P. C. Nelson, Y. E. Goldman, Tilting and wobble of myosin V by high-speed single-molecule polarized fluorescence microscopy. *Biophys. J.* **104**, 1263–1273 (2013).
21. O. Zhang *et al.*, Six-dimensional single-molecule imaging with isotropic resolution using a multi-view reflector microscope. *Nat. Photon.* **17**, 179–186 (2023).
22. S. B. Mehta *et al.*, Dissection of molecular assembly dynamics by tracking orientation and position of single molecules in live cells. *Proc. Natl. Acad. Sci. U.S.A.* **113**, E6352–E6361 (2016).
23. V. Swaminathan *et al.*, Actin retrograde flow actively aligns and orients ligand-engaged integrins in focal adhesions. *Proc. Natl. Acad. Sci. U.S.A.* **114**, 10648–10653 (2017).
24. Y. Wu *et al.*, Spatially isotropic four-dimensional imaging with dual-view plane illumination microscopy. *Nat. Biotechnol.* **31**, 1032–1038 (2013).
25. T. Chandler, S. Mehta, H. Shroff, R. Oldenbourg, P. J. La Rivière, Single-fluorophore orientation determination with multiview polarized illumination: Modeling and microscope design. *Opt. Express* **25**, 31309–31325 (2017).
26. P. J. Basser, J. Mattiello, D. Le Bihan, MR diffusion tensor spectroscopy and imaging. *Biophys. J.* **66**, 259–267 (1994).
27. D. S. Tuch, Q-ball imaging. *Magn. Reson. Med.* **52**, 1358–1372 (2004).
28. T. Chandler, H. Shroff, R. Oldenbourg, P. J. La Rivière, Spatio-angular fluorescence microscopy I. Basic theory. *J. Opt. Soc. Am. A* **36**, 1334–1345 (2019).
29. T. Chandler, H. Shroff, R. Oldenbourg, P. J. La Rivière, Spatio-angular fluorescence microscopy II. Paraxial 4*f* imaging. *J. Opt. Soc. Am. A* **36**, 1346–1360 (2019).
30. T. Chandler, H. Shroff, R. Oldenbourg, P. J. La Rivière, Spatio-angular fluorescence microscopy III. Constrained angular diffusion, polarized excitation, and high-NA imaging. *J. Opt. Soc. Am. A* **37**, 1465–1479 (2020).
31. J. Myšková *et al.*, Directionality of light absorption and emission in representative fluorescent proteins. *Proc. Natl. Acad. Sci. U.S.A.* **117**, 32395–32401 (2020).
32. Y. Wu *et al.*, Reflective imaging improves spatiotemporal resolution and collection efficiency in light sheet microscopy. *Nat. Commun.* **8**, 1452 (2017).
33. J. Cheng, P. J. Basser, Director field analysis (DFA): Exploring local white matter geometric structure in diffusion MRI. *Med. Image Anal.* **43**, 112–128 (2018).
34. S. Abrahamsson *et al.*, Multifocus polarization microscope (MF-Polscope) for 3D polarization imaging of up to 25 focal planes simultaneously. *Opt. Express* **23**, 7734–7754 (2015).
35. J. Thomas, N. A. Idris, D. A. Collings, Pontamine fast scarlet 4B bifluorescence and measurements of cellulose microfibril angles. *J. Microsc.* **268**, 13–27 (2017).
36. T. Ushiki, Collagen fibers, reticular fibers and elastic fibers. A comprehensive understanding from a morphological viewpoint. *Arch. Histol. Cytol.* **65**, 109–126 (2002).
37. M. Fernández *et al.*, Small-angle x-ray scattering studies of human breast tissue samples. *Phys. Med. Biol.* **47**, 577 (2002).
38. A. D. Doyle, N. Carvajal, A. Jin, K. Matsumoto, K. M. Yamada, Local 3D matrix microenvironment regulates cell migration through spatiotemporal dynamics of contractility-dependent adhesions. *Nat. Commun.* **6**, 1–15 (2015).

39. M. W. Conklin *et al*., Aligned collagen is a prognostic signature for survival in human breast carcinoma. *Am. J. Pathol.* **178**, 1221–1232 (2011).
40. B. Weigelin, G. J. Bakker, P. Friedl, Intravital third harmonic generation microscopy of collective melanoma cell invasion: Principles of interface guidance and microvesicle dynamics. *Intravital* **1**, 32–43 (2012).
41. A. G. Clark, D. M. Vignjevic, Modes of cancer cell invasion and the role of the microenvironment. *Curr. Opin. Cell Biol.* **36**, 13–22 (2015).
42. A. Glentis *et al*., Cancer-associated fibroblasts induce metalloprotease-independent cancer cell invasion of the basement membrane. *Nat. Commun.* **8**, 1–13 (2017).
43. E. N. Taylor, M. P. Hoffman, G. E. Aninwene II, R. J. Gilbert, Patterns of intersecting fiber arrays revealed in whole muscle with generalized Q-space imaging. *Biophys. J.* **108**, 2740–2749 (2015).
44. A. D. Doyle, F. W. Wang, K. Matsumoto, K. M. Yamada, One-dimensional topography underlies three-dimensional fibrillar cell migration. *J. Cell Biol.* **184**, 481–490 (2009).
45. S. P. Carey, C. M. Kraning-Rush, R. M. Williams, C. A. Reinhart-King, Biophysical control of invasive tumor cell behavior by extracellular matrix microarchitecture. *Biomaterials* **33**, 4157 (2012).
46. B. A. C. Harley *et al*., Microarchitecture of three-dimensional scaffolds influences cell migration behavior via junction interactions. *Biophys. J.* **95**, 4013–4024 (2008).
47. S. Durgam, B. Singh, S. L. Cole, M. T. Brokken, M. Stewart, Quantitative assessment of tendon hierarchical structure by combined second harmonic generation and immunofluorescence microscopy. *Tissue Eng. Part C Methods* **26**, 253–262 (2020).
48. P. Friedl, K. Wolf, Plasticity of cell migration: A multiscale tuning model. *J. Cell Biol.* **188**, 11–19 (2010).
49. K. Sheets, S. Wunsch, C. Ng, A. S. Nain, Shape-dependent cell migration and focal adhesion organization on suspended and aligned nanofiber scaffolds. *Acta Biomater.* **9**, 7169–7177 (2013).
50. A. Jana *et al*., Crosshatch nanofiber networks of tunable interfiber spacing induce plasticity in cell migration and cytoskeletal response. *FASEB J.* **33**, 10618–10632 (2019).
51. A. Jana *et al*., Mitotic outcomes and errors in fibrous environments. *Proc. Natl. Acad. Sci. U.S.A.* **120**, e2120536120 (2023).
52. K. Schakenraad *et al*., Mechanical interplay between cell shape and actin cytoskeleton organization. *Soft Matter* **16**, 6328–6343 (2020).
53. J. Huisken, D. Y. R. Stainier, Even fluorescence excitation by multidirectional selective plane illumination microscopy (MSPIM). *Opt. Lett.* **32**, 2608–2610 (2007).
54. J. Lazar, A. Bondar, S. Timr, S. J. Firestein, Two-photon polarization microscopy reveals protein structure and function. *Nat. Methods* **8**, 684–690 (2011).
55. N. Nakai *et al*., Genetically encoded orientation probes for F-actin for fluorescence polarization microscopy. *Microscopy* **68**, 359–368 (2019).
56. T. P. Burghardt, Time-resolved fluorescence polarization from ordered biological assemblies. *Biophys. J.* **48**, 623–631 (1985).
57. K. Suhling *et al*., Time-resolved fluorescence anisotropy imaging applied to live cells. *Opt. Lett.* **29**, 584–586 (2004).
58. A. Volpato *et al*., Extending fluorescence anisotropy to large complexes using reversibly switchable proteins. *Nat. Biotechnol.* **41**, 1–8 (2022).
59. N. Karedla *et al*., Simultaneous measurement of the three-dimensional orientation of excitation and emission dipoles. *Phys. Rev. Lett.* **115**, 173002 (2015).
60. F. T. S. Chan, C. F. Kaminski, G. S. K. Schierle, HomoFRET fluorescence anisotropy imaging as a tool to study molecular self-assembly in live cells. *ChemPhysChem* **12**, 500–509 (2011).
61. M. L. Markwardt *et al*., A genetically encoded biosensor strategy for quantifying non-muscle myosin II phosphorylation dynamics in living cells and organisms. *Cell Rep.* **24**, 1060–1070.e4 (2018).
62. T. Chandler *et al*., Three-dimensional spatio-angular fluorescence microscopy with a polarized dual-view inverted selective-plane illumination microscope (pol-diSPIM). BioStudies. https://www.ebi.ac.uk/biostudies/bioimages/studies/S-BIAD1055. Deposited 12 March 2024.
63. M. Guo, micoImageLib. Github. https://github.com/eguomin/microImageLib. Accessed 12 March 2024.
64. T. Chandler, polaris. Github. https://github.com/talonchandler/polaris. Accessed 12 March 2024.